Chemical Engineering Science 190 (2018) 149–163

Contents lists available at ScienceDirect

Chemical Engineering Science

journal homepage: www.elsevier.com/locate/ces

Liquid residence time distribution of multiphase horizontal flow in packed bed milli-channel: Spherical beads versus open cell solid foams

Marion Serres [a,b,1], Daniel Schweich [a], Valérie Vidal [b], Régis Philippe [a,*]

[a] Laboratoire de Génie des Procédés Catalytiques (UMR 5285), CNRS, CPE Lyon, UCBL, Université de Lyon, F-69616 Villeurbanne, France
[b] Laboratoire de Physique (UMR 5672), CNRS, ENS de Lyon, Université de Lyon, F-69342 Lyon, France

HIGHLIGHTS

- Robust access to liquid RTD in small-scale porous packings under multiphase flow conditions is presented.
- Dense micro-packed beds are compared to open cell solid foams.
- A modified liquid hold up correlation is developed and is valid for both packings.
- RTD broadening is explained by a combination of convective dispersion and mass transfer to a fraction of immobile liquid.

GRAPHICAL ABSTRACT

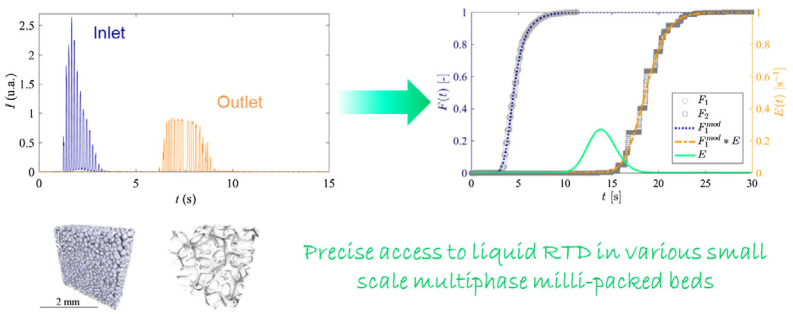

ARTICLE INFO

Article history:
Received 22 January 2018
Received in revised form 13 April 2018
Accepted 2 May 2018

Keywords:
Multiphase flow
Milli-channel
Packed bed
Open cell solid foam
Hydrodynamics
Segmented Taylor flows

ABSTRACT

A robust approach to access liquid residence time distribution (RTD) adapted to multiphase flow in porous media is presented. It is tailored to meet specific requirements of small scale systems (centimeter, millimeter or less) with Taylor segmented flow feed. The method involves direct visualization using fluorescence microscopy close to both extremities of a porous packing. Critical image treatment steps and optimization of a versatile discrete model with 4 parameters are detailed and discussed. They allow the precise and rapid determination of RTD curves and their 1st- and 2nd-order moments. The application of the method is successfully illustrated with dense micro-packed beds of sub-millimeter particles and highly porous media like open cell solid foams undergoing a preformed G-L segmented (Taylor) flow. Original results regarding the effect of fluid flowrates and different confined porous media are discussed and lead to a single two-parameter liquid hold up correlation, which is valid for both packings. As usual, RTD broadening is treated as a combination of convective dispersion and mass transfer to a fraction of immobile liquid. The predominant role of mass transfer is underlined with an analysis of characteristic times.

1. Introduction

Micro- or milli-packed beds (MPBs) of small catalyst particles (10–200 μm) became established and efficient lab-tools in the case of heterogeneously catalyzed gas–liquid (G-L) reactions (Losey et al., 2001; van Herk et al., 2005; Al-Rifai et al., 2016; Moulijin et al., 2016, Faridkhou et al., 2016). Their attractive mass and heat transfer performances and their low material inventory are the driving reasons for this development. Overall, they help speeding up the access to intrinsic chemical activity (van Herk et al., 2009) and optimizing operating conditions in potentially unconventional and risky domains where macroscale reactors are difficult to operate (Inoue et al., 2007). Additionally, these tools can be of great

* Corresponding author.
E-mail address: regis.philippe@lgpc.cpe.fr (R. Philippe).
[1] Current adress: IFP Energies nouvelles, Rond-point de l'échangeur de Solaize, F-69360 Solaize, France.

https://doi.org/10.1016/j.ces.2018.05.004
0009-2509/

Nomenclature

$CV_{\tilde{t}_{exp}}$	variation coefficient of the 1st-order moment of the RTD [%]
$CV_{\sigma^2_{exp}}$	variation coefficient of the 2nd-order moment of the RTD [%]
d	spherical particle diameter [m]
d_{pore}	mean cell (OCSFs) or pore (MPB) diameter [m]
$E(t)$	residence time distribution function [s^{-1}]
$\bar{E}(s)$	Laplace transform of the RTD [-]
$E_R(\theta)$	RTD in reduced time coordinate [–]
$\overline{E_R}(s)$	Laplace transform of the RTD in reduced time coordinate [–]
$F_{l,\,i}\,(t)$	cumulative raw tracer intensity [a.u.]
$F_i\,(t)$	cumulative tracer intensity after baseline correction [a.u.]
$F_i^{mod}(t)$	modelled cumulative tracer intensity [a.u.]
$\overline{F_i^{mod}}(s)$	modelled cumulative tracer intensity in Laplace domain [–]
h	channel height [m]
$I_i(t)$	raw tracer intensity [a.u.]
J	number of mixing cells in series [–]
K_{im}	ratio of immobile to mobile liquid fractions [–]
of	objective function [–]
Q_i	volumetric flowrate of fluid i [m^3/s]
r	radius of the gas injection channel [m]
s	Laplace variable [s^{-1}]
S_L	liquid saturation in the porous media [–]
$\tilde{t}$	first-order moment of the RTD [s]
$\tilde{t}_i$	first-order moment of curve i [s]
t_m	residence time of the mobile liquid phase [s]
t_M	mass transfer time between mobile and stagnant zones [s]
t_D	characteristic time of hydrodynamic dispersion in the mobile zone [s]
t_T	characteristic time of mass transfer between static and dynamic zones [s]
u_i	superficial velocity of the fluid i [m/s]
u_{DF}	drift flux velocity [m/s]
V	volume of liquid [m^3]
$\vec{v}_i$	Eigenvectors of the variance-covariance matrix (i = 1–4) [–]
V_R	volume of the reactor [m^3]

Greek symbols:

α, β	parameters of the drift flux model by Molga and Westerterp (1997) [–]
α', β'	parameters of the adapted drift flux model [–]
γ	surface tension [N/m]
δ	distance from channel wall [m]
δ_F	residuals between the model and experimental outlet F_2 curves [–]
ε	volume averaged foam or bed porosity [–]
$\varepsilon\delta$	mean porosity at a distance δ from the channel walls [–]
ε_{bulk}	mean porosity far from the walls [–]
ε^*	reduced porosity, $\varepsilon\delta/\varepsilon_{bulk}$ [–]
ε_L	liquid hold up of the reactor [–]
ε_L^{mod}	liquid hold up estimated from the drift flux model [–]
θ	reduced time coordinate, $t/\tilde{t}$ [–]
θ_m	fraction of mobile liquid phase [–]
θ_{im}	fraction of immobile or stagnant liquid phase [–]
μ	viscosity [–]
ρ	density [kg/m^3]
σ^2	variance of the RTD [s^2]
σ_i^2	variance of the curve i [s^2]
σ'^2	reduced variance of the RTD [s^2]

Subscripts:

0	initial values
1	inlet
2	outlet
DF	drift flux
exp	experimental
G	gas
L	liquid
min	minimum
max	maximum
mod	model
R	reactor, reduced.
S	solid

Abbreviations:

$CSTR_4$	series of continuously stirred tank reactor model with 4 parameters
FFT	fast Fourier transform
LHS	Latin hypercube sampling
MPB	micro packed bed
OCSF	open cell solid foam
PPI	pores per inch
RTD	residence time distribution

interest to mimic and understand the complex two-phase flow patterns occurring at intergranular pore scale in larger scale reactors.

For production purpose, this concept faces scalability and operability issues inherent to multiple channel geometries. Important pressure drop, clogging, uniform two-phase distribution, reproducible loading, catalytic bed replacement and heat exchange integration are among them. Nonetheless, several examples are reported in the literature with reliable small production throughput (Plucinski et al. 2005; Lerou et al., 2010; Deshmukh et al. 2010; Inoue et al. 2015).

Recently, milli-channels containing alternative porous structures like pillar arrays (de Loos et al., 2010; Yang et al., 2015), open-cell solid foams (Saber et al. 2012; Liu et al. 2013; Tourvieille et al. 2015, 2015a) or ordered porous media (Häfeli et al., 2013; Elias and von Rohr, 2016; Potdar et al. 2017) have been reported for multiphase applications. All these internals still exhibit very good mass transfer and reaction performances but with drastically reduced pressure drop which can be attractive for future lab-tools or millireactor concepts.

At millimeter scale, in a wide range of feeding conditions and in empty channels, gas-liquid flows are often self-organized as segmented flows (also well-known as Taylor flows) (Kreutzer et al., 2005a, 2005b). A global understanding of the progressive disorganization of this flow entering porous beds (spheres, foams, etc.) is of fundamental importance because it governs the phase ratio, local mixing, the gas-liquid contact surface area and eventually the mass transfer performance. Residence Time Distribution (RTD) measurements provide precious and meaningful information (mean residence time and phase hold up of each fluid phase, dispersive behavior, presence of dead-zones or by-pass, etc.) about these issues. It helps handling and modeling the spreading of the reactants and products along the reactor which can lead to selectivity and conversion issues.

RTD acquisition at small scale is challenging and various artefacts can alter its proper determination (Faridkhou et al., 2013):

- The use of classical probes developed for larger volume reactors can yield biased results owing to large dead volumes that affect at least the mean residence time and the variance of the RTD. Typically, a precision of a few percent on the mean residence time requires that the probe volume is less than a few percent of the volume accessible for the fluid. For a milli-reactor of several hundreds of μL, as the one used in the present study, this implies using a probe of less than few μL.
- Whatever the probe, the specific "pulsed" nature of a G-L segmented flow inside milli-channels leads to pulsed raw experimental signals. Recovering the RTD from these signals represents a technical challenge.
- Most often, the inlet tracer signal is not recorded and is assumed to be an ideal one (Dirac pulse, instantaneous step) without experimental evidence of the validity or consequence of the assumption (van Herk et al., 2005; Marquez et al., 2008; Kulkarni and Kalyani, 2009).
- A G-L separator is often inserted between the reactor outlet and the tracer sensor (van Herk et al., 2005, Marquez et al., 2008) that again induces an extra volume and a disturbance of the liquid flow.

To overcome most of these problems, Tourvieille et al. (2015) have presented a two-measurement technique based on direct visualization using fluorescence microscopy at both ends of a porous packing. It was an adaptation of the technique developed by Trachsel et al. (2005) and Kreutzer et al. (2008) for empty microchannels without practical details for precise signal processing. As will be discussed hereafter, the signal processing developed in the work of Tourvieille et al. (2015) gave access to the signal envelopes and can be subject to a small bias. Thus, the first original objective of this work is to present and discuss a new consolidated image processing method including its robustness and applicability limits. The second original objective is to propose a comparison of two different milli-channel packings fed with a G-L segmented flow: "conventional" dense packed beds of spherical particles and open cell solid foams. The impact of gas and liquid flow rates on the RTD is studied for different samples of each porous structure. The analysis of the first-order moments of the RTD curves makes it possible to quantify an original correlation between the liquid hold up and the feed conditions whatever the packing. Examination of the second-order moments supports a discussion on the predominant processes of dispersion and their evolution with different operating conditions.

2. Experimental procedures

2.1. Cell design

The cell consists of a horizontal square channel of $h = 2$ mm width (cross-section $h \times h = 4$ mm^2) and a total length of 24 cm, drilled in PEEK (PolyEther Ether Ketone) (Fig. 1a). The top wall is a glass plate that allows direct visualization of the tracer (see Section 2.3). To ensure the same surface properties on the channel walls, a thin (10 nm) layer of diamond-like carbon is coated by plasma deposition. Two types of porous media are studied: spherical beads (MPBs) and Open Cell Solid Foams (OCSFs) (see details in Section 2.2). They occupy the whole section of the channel along 15 cm for the MPBs and 16 cm for the OCSFs.

Pure nitrogen and ethanol are used as model fluids (fluid properties are listed in Table 1) and are delivered at ambient temperature and pressure using respectively a mass flow controller (Analyt MTC) and a syringe pump (Harvard apparatus PHD 4400) equipped with a stainless steel 50 mL syringe. Flow rates are chosen in the range 0.5–8.0 mL/min for the liquid and 2.0–35 mL/min for the gas (always in normal conditions). The liquid flow is injected directly in the main channel while the gas flow is supplied perpendicularly through a narrow circular lateral channel (radius $r = 0.5$ mm), forming a T-junction and allowing the formation of a G-L segmented flow 2 cm upstream of the porous medium entrance (Fig. 1).

2.2. Porous media

Two types of porous media are investigated: (1) Milli-Packed Beds [MPB 75 (Fig. 2a) and MPB 180 (Fig. 2b)] made of poly-

Table 1
Main physical characteristics of the liquid (L) and gas (G) phases at 293 K and 1 atmosphere. The ethanol-nitrogen surface tension is $\gamma \approx 22$ mN/m (Dittmar et al., 2003).

	Ethanol (L)	Nitrogen (G)
Density ρ [kg/m^3]	795	1.15
Viscosity μ [mPa s]	1.15	1.76×10^{-2}

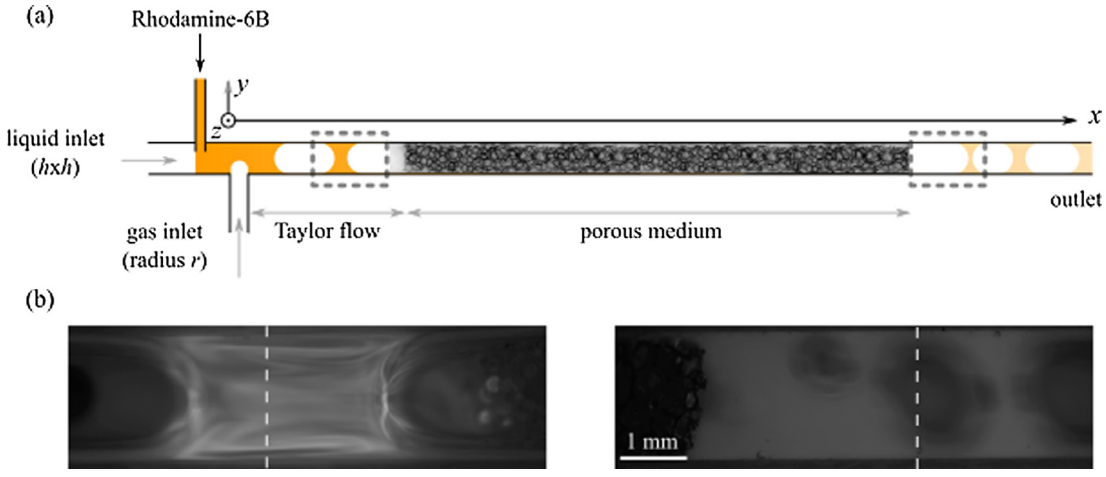

Fig. 1. (a) Schematic top view of the reactor. A segmented gas–liquid flow is created upstream the porous medium in a square channel of 2 mm × 2 mm cross-section and total length of 24 cm. (b) Rhodammine-6B is injected in the liquid phase, and its fluorescence intensity is measured upstream (left) and downstream (right) of the porous medium (dashed rectangles in (a)) along a single line of pixels (dashed white lines). Further image processing allows computing the Residence Time Distribution (RTD).

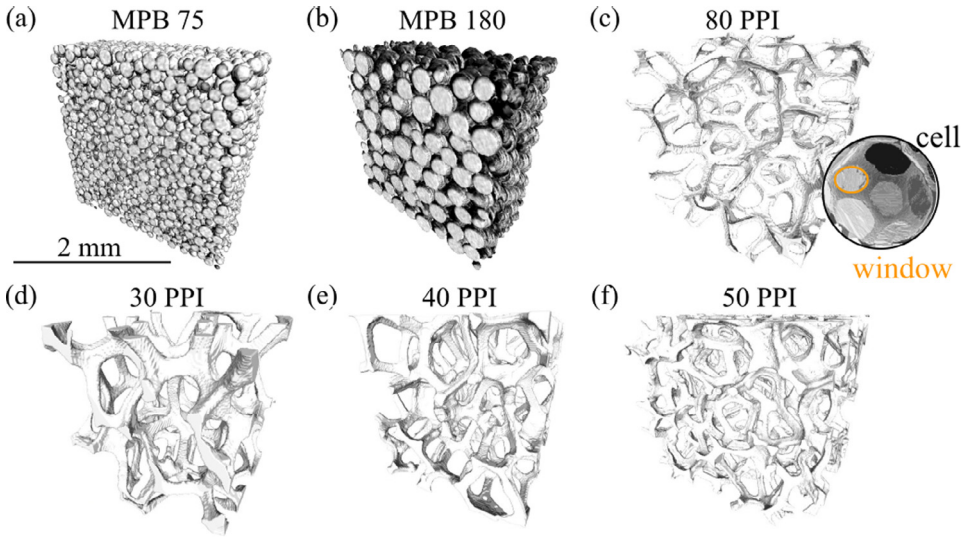

Fig. 2. X-ray tomography 3D images of the different porous media: (a) MPB 75, (b) MPB 180, (c) 80 PPI foam with the illustration of the difference between cells (cage surrounded by struts) and windows (junction between two cells), (d) 30 PPI foam, (e) 40 PPI foam, (f) 50 PPI foam.

dispersed spherical glass particles and (2) Open Cell Solid Foams (OCSFs) made of either vitreous carbon [80 PPI, ERG-Aerospace, (Fig. 2c)] or nickel-chrome alloy (Ni-Cr) [30 PPI, 40 PPI, 50 PPI, Recemat (Fig. 2d, e, f)]. The particles of the milli-packed beds are maintained by a downstream plug made of a 2 cm long piece of foam (NiCr, 50 PPI), whereas the upstream end is a free surface. Foams are precisely cut with electro-erosion technique to form $2 \times 2 \times 20$ mm bars and 8 of them are inserted inside the milli-channel to build the porous medium. These six porous media have been analyzed by X-ray tomography (GE Phoenix v|tome|x s, RX tube of 160 kV with focal point of up to 1 µm) with a spatial resolution of 5 µm. Tomographic data are processed with iMorph® software (Brun et al., 2008) providing illustrative 3D images of each medium (Fig. 2), radial porosity profiles (Fig. 3) and a precise quantification of the structure (Table 2).

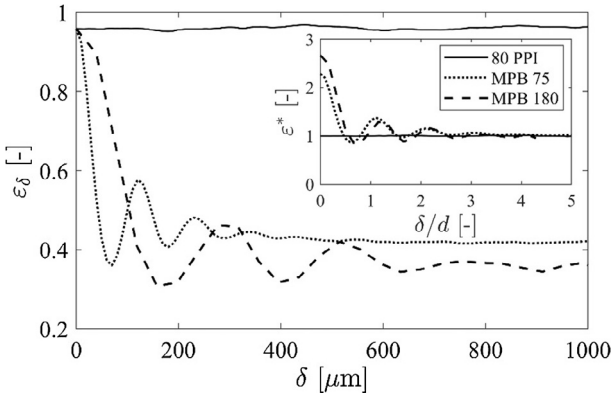

Fig. 3. Porosity profile $\varepsilon\delta$ as a function of the distance δ from the channel walls for a typical foam (80 PPI, solid line) and the two micropacked beds (MPB 75, dotted line, and MPB 180, dashed line). *Inset:* dimensionless porosity profile, $\varepsilon^* = \varepsilon\delta \,/\, \varepsilon_{bulk}$, where ε_{bulk} is the mean porosity far from the walls, as a function of δ/d, where d is the mean particle diameter for MPBs and the mean window diameter for OCSFs. Note that the wavelength of the porosity oscillation is close to the mean particle diameter, d for the MPBs.

MPBs are mainly characterized by their (number averaged) mean particle diameter (d) given in the rightmost column of Table 2. OCSFs are commercially described by a coarse linear pore density expressed in Pores Per Inch (PPI). Nonetheless, (number averaged) mean window-, cell- and strut-diameters are more relevant and useful for a precise characterization. The cells correspond to the void cages enclosed by the struts whereas windows consist of common faces (not necessarily planar) between two adjacent cells (Fig. 2c). To compare the different porous media, common parameters are chosen: the bed porosity (ε) and the (number averaged) mean pore diameter (d_{pore}). For MPBs, because of an insufficient spatial resolution, this last parameter cannot be extracted from the X-ray tomography measurements. It is estimated as 20% of the mean particle diameter (Glover and Walker, 2009; Varas et al. 2011). In the case of foams, the mean pore diameter is taken as the mean window diameter, computed from X-ray tomography and image processing (Table 2). The identical mean pore diameters computed for the 40 PPI and 80 PPI foams illustrate the poor significance of the linear pore density as defined by the foam supplier.

In Fig. 3, the porosity $\varepsilon\delta$ is plotted as a function of the distance δ from the wall of the channel, for different porous media. It is obtained by averaging the porosity between δ and δ+dδ from the channel walls, over the whole analyzed medium. Fig. 3 inset presents the same porosity profiles in reduced coordinates where the reduced porosity ε^* is the porosity $\varepsilon\delta$ normalized by ε_{bulk}, the mean porosity far from the walls, close to the center of the channel,

Table 2
Characteristics of the different porous media from X-ray tomography: porosity ε, pore diameter d_{pore}, particle diameter d.

Name	Type	Material	ε [–]	d_{pore} [µm]	d [µm]
MPB 75	Spheres	Glass	0.44	19 ± 6	93 ± 25
MPB 180	Spheres	Glass	0.40	41 ± 12	206 ± 59
80 PPI	Foam	Carbon	0.960 ± 0.003	257 ± 85	–
30 PPI	Foam	NiCr	0.899 ± 0.014	386 ± 120	–
40 PPI	Foam	NiCr	0.895 ± 0.007	257 ± 87	–
50 PPI	Foam	NiCr	0.891 ± 0.016	168 ± 63	–

and the distance δ is normalized by the bead or cell diameter, d. In the case of foams (here illustrated only for the 80PPI foam), it is noticeable that the porosity profile present no variations and $\varepsilon_{bulk} = \varepsilon$ because the structure of the material is quite uniform. Conversely, the two bead packings are constrained by the wall, which induces damped porosity oscillations with a wavelength close to the bead diameter d (Fig. 3 inset). This behavior was largely and formerly studied in the literature (Mueller, 1991; Papageorgiou and Froment, 1995; de Klerk, 2003) for classical tubular fixed beds. The porosity of the MPBs, ε, which is used later on, is taken as the volume averaged mean porosity over the whole channel.

2.3. Data acquisition & processing

The Residence Time Distribution (RTD) is obtained from a pulse injection of a Rhodamine-6B, (Sigma-Aldrich, 99%) solution at a concentration of 3.2×10^{-5} mol L^{-1} in the liquid phase, upstream of the T-junction as in the work of Tourvieille et al. (2015). Reproducible pulse injections are obtained using a 5 µL loop mounted on a switching 6-way valve (Rheodyne 7725i). Tracer signals are recorded by direct visualization of the fluorescent dye intensity (Fig. 1b) using a fluorescence microscope (Olympus BX51M equipped with a 2.5x objective) combined with a high speed camera (Solinocam H2D2, 113 frames per second). The movies are processed with Matlab™ (Mathworks®) in order to extract the dye intensity raw signals versus time (Fig. 4a). Because tracer injections are not ideal Dirac pulses, two signals are acquired, $I_1(t)$ at the inlet and $I_2(t)$ at the outlet of the porous medium (later on, index 1 always refers to the inlet and 2 to the outlet). As it was not possible to acquire both signals simultaneously, successive experiments are performed with the same stationary Taylor flow conditions. Four tracer injections for each set of experimental conditions ensure a testing of the reproducibility which yields four (I_1, I_2) couples. This non-invasive visualization technique close to the packing ends avoids dead volume of in-situ sensors that are detrimental to signal quality in so small devices. As discussed in the introduction, contrary to smooth tracer signals obtained in single phase flows, the signals are spiky and pulsed due to the Taylor flow (Fig. 4a). Recovering the RTD from such signals is challenging and cannot be done through direct deconvolution of the outlet and inlet signals. As discussed in the introduction, Tourvieille et al. (2015) bypassed this problem by a smoothing treatment that defines the RTD from the envelope of the peaks (Fig. 4b). Thus, "envelope-smoothed" inlet and outlet tracer responses can be further processed by deconvolution. This processing appears physically disputable because tracer mass balance is not fulfilled, and it can lead to inaccurate RTD curves of the liquid phase. Indeed, integrals under the envelope curves overestimate the liquid phase contribution due to the flowing gas (Fig. 4b).

Therefore, a new processing method that preserves tracer mass balance is introduced as follows: The raw pulsed tracer signals $I_i(t)$ (Fig. 5a and b, solid orange lines) are integrated, providing cumulative raw intensity curves $F_{I,i}(t)$ (Fig. 5a and b, dashed lines). The baseline drifts observed in these curves are the result of the random and stationary optical noise (light reflections on the gas bubbles as described in Buttler et al. (2016)). Thus, after baseline correction on the $F_{I,i}(t)$ curves (by subtracting the linear drift due to the noise) and a normalization to unity, "cleaned" inlet and outlet cumulative experimental signals are obtained and are hereafter named $F_i(t)$ (Fig. 5a-b, solid blue lines). The tracer mass balance in these signals is preserved because of the stationarity of the noise in the experiments and its independence of the tracer concentration. Classically, a deconvolution method – for instance via a Fast Fourier Transform (FFT method) – is used to extract the RTD from F_1-F_2 couple (Trachsel et al., 2005; Hutter et al., 2011; Saber et al., 2012; Tourvieille et al., 2015). However, deconvolution is an improper mathematical operation, very sensitive to noise in the raw signals. It may yield biased unphysical results (oscillating RTD, negative tracer concentration) or is even unstable. The problem is avoided here by developing a more robust method based on two steps:

- Smoothing of the $F_1(t)$ curve with a suitable expression to obtain $F_1^{mod}(t)$; At that point, there is no physical interpretation, but only smoothing.
- Fitting of the parameters of a versatile RTD model to reproduce as closely as possible the F_2 curve at outlet by direct convolution (proper and more robust mathematical operation) of $F_1^{mod}(t)$ by the RTD model. The next section describes this new method and the RTD model in details.

3. Modeling

3.1. Model formulation

When looking at a F curve (as the solid blue lines in Fig. 5), one easily recognizes the response of a dispersive plug flow, at least from a qualitative point of view. Unless dispersion is very high, the corresponding RTD is almost symmetrical. The more or less pronounced asymmetry around the mid-point observed in Fig. 5

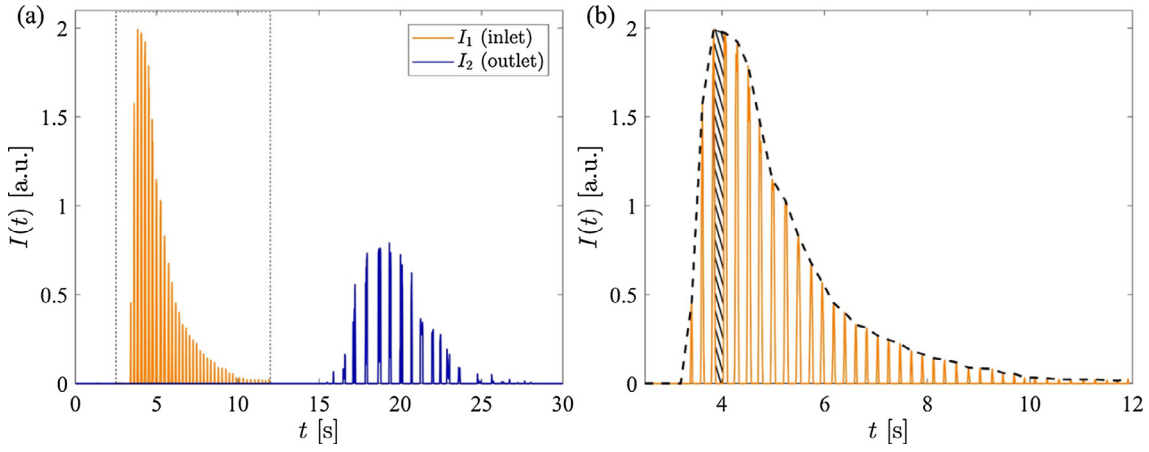

Fig. 4. (a) Typical inlet (orange) and outlet (dark blue) raw pulsed signals (in arbitrary units) obtained from direct visualization [80PPI foam, Q_G = 10 mL/min, Q_L = 2 mL/min]. The dashed rectangle corresponds to the zoom in (b). (b) Zoom on the inlet signal and illustration of the bias induced by considering the envelope curve: the hatched area between two successive peaks of tracer represents an extra-area (gas bubble) that is wrongly taken into account.

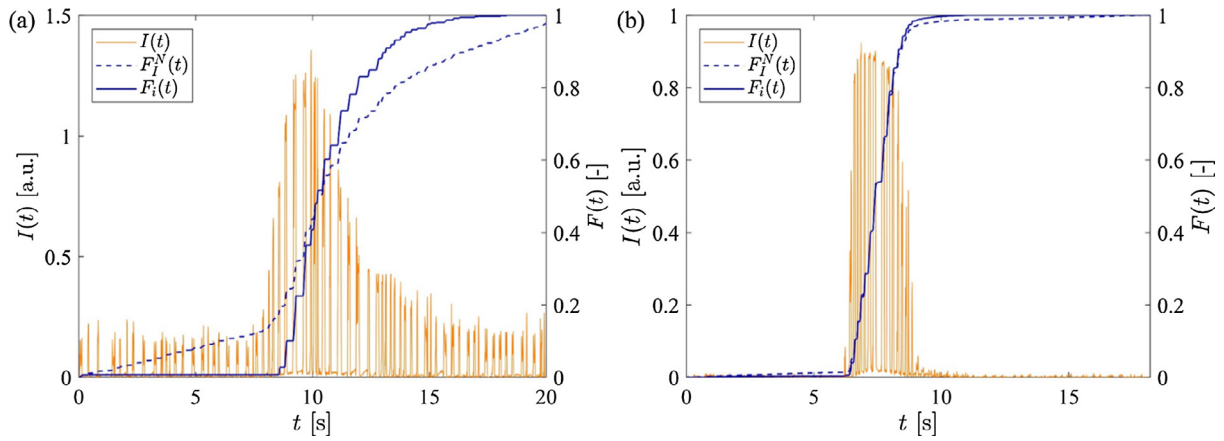

Fig. 5. Processing of the experimental signal that leads to corrected curves. $I(t)$ is the raw pulsed signal (in arbitrary units, orange solid line); $F_I(t)$ is the cumulative raw signal (dark blue dashed line) and $F(t)$ the cumulative of the final signal corrected from the non-zero and noisy baseline (solid dark blue line). Both panels display examples of inlet signal for the 80 PPI foam for (a) Q_G = 10 mL/min, Q_L = 4 mL/min and (b) Q_G = 8 mL/min and Q_L = 6 mL/min.

suggests the presence of a stagnant zone. Simple models for dispersive flow with or without stagnant zones are plethora in the literature (see Danckwerts, 1953, Wen and Fan, 1975, Sardin et al., 1991, Stegeman et al., 1996, Iliuta et al., 1999). The model used in this study is a discrete series of continuous mixing cells containing a stagnant zone and is schematically illustrated in Fig. 6 (hereafter named $CSTR_4$). It is a simple alternative to the classical dispersive flow model based on Fick's law. Common sense suggests that this versatile model should easily mimic the flow pattern from the injection of Rhodamine dye down to the inlet detection zone and then through the reactor zone either packed with beads or foams, although *it does not necessarily represent the true physical processes responsible for tracer dispersion*. This model has been used also by Tourvieille et al. (2015) in the case of multiphase flow in open cell solid foam and gave good estimates of the RTD.

Let V be the volume of liquid in the system under study. As described by Sardin et al. (1991), each mixing cell contains a volume $V \times \theta_m/J$ of mobile (i.e., flowing) liquid, and a volume $V \times \theta_{im}/J$ of stagnant liquid, where θ_m and θ_{im} are the fraction of mobile and immobile liquid respectively ($\theta_m + \theta_{im} = 1$) and J is the number of mixing cells. It has been shown that the Laplace transform of the RTD, $E(t)$, of this system is:

$$\bar{E}(s) = \left\{1 + \frac{st_m}{J}\left[1 + \frac{K_{im}}{1 + st_M}\right]\right\}^{-J} \tag{1}$$

where t_m is the residence time of the mobile liquid phase and accounts for convection, t_M is the characteristic time of transfer between mobile and immobile liquid, accounting for both external and internal transfer (for more details see Villermaux (1987) and Sardin et al. (1991)), and $K_{im} = \theta_{im}/\theta_m$ is the ratio of the immobile over mobile fraction of the liquid phase. The first-order moment ($\tilde{t}$) and the second-order centered and reduced moment (σ'^2) of this E distribution function are given by Sardin et al. (1991) using the parameters of this $CSTR_4$ model:

$$\tilde{t} = t_m(1 + K_{im}) \tag{2}$$

$$\sigma'^2 = \frac{\sigma^2}{\tilde{t}^2} = \frac{1}{J} + \frac{2K_{im}}{1 + K_{im}}\frac{t_M}{\tilde{t}} \tag{3}$$

In order to discuss and compare the RTD curves and in particular to decouple the second-order moment from its dependence on the mean residence time, it is often helpful to use a reduced time (θ) for the RTD and the corresponding reduced RTD expression ($E_R(\theta)$). The Laplace transform of this reduced RTD model in reduced time coordinate is then given by:

$$\theta = \frac{t}{\tilde{t}} = \frac{t}{t_m(1 + K_{im})} \tag{4}$$

$$\overline{E_R}(s) = \left\{1 + \frac{s}{J(1 + K_{im})}\left[1 + \frac{K_{im}}{1 + s\frac{t_M}{t_m(1+K_{im})}}\right]\right\}^{-J} \tag{5}$$

3.2. Smoothing of inlet F_1 curves

The first modelling step described in Section 2.3, consists in using the model to smooth the baseline-corrected F_1 curve with no possibility of oscillations as often encountered with purely mathematical and blind smoothing procedures. The global non-linear parameter regression is performed using a Levenberg-Marquardt algorithm (Matlab™, Mathworks®) associated with a variation of the initial conditions in order to avoid any "local" solution due to the presence of four regressed parameters (see Appendix A). Fig. 7 shows an example of the excellent agreement between the model smoothed curve $F_1^{mod}(t)$ according to this $CSTR_4$ model, and the baseline-corrected $F_1(t)$ signal normalized to unity. In the present case, the four model parameters have no physical meaning, as there is no evidence that the physical phenomena described in the model are responsible for the shape on the inlet

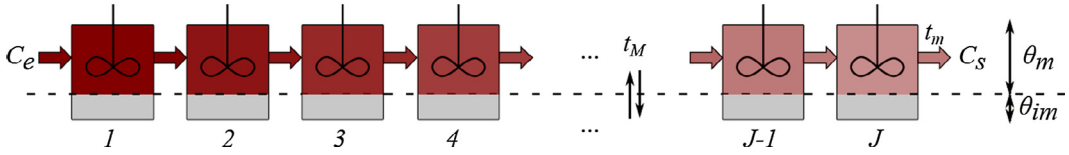

Fig. 6. Sketch of the $CSTR_4$ model characterized by a cascade of J identical cells, C_e and C_s are the tracer concentration at the entrance and the outlet of the porous medium respectively. Each single cell contains a fraction of mobile (θ_m) and immobile (θ_{im}) liquid. t_m and t_M are respectively the residence time of the mobile liquid fraction and the time for mass transfer between the mobile and immobile zones.

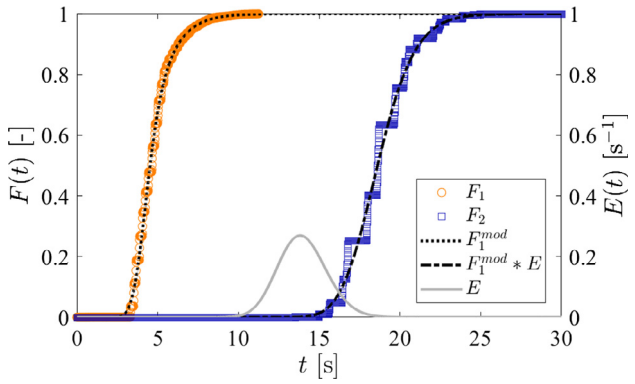

Fig. 7. Example of the inlet raw signal (F_1) fitting obtained with the CSTR$_4$ model (F_1^{mod}), the result of the convolution method ($F_1^{mod} * E$) and the RTD (E) [80 PPI foam, Q_G = 10 mL/min and Q_L = 2 mL/min].

signals. Conversely, they allow recovering the leading moments of the F_1 curve using Eqs. (2) and (3). More important for the next step, any residual baseline drift, or noise (stepwise increase due to the segmented flow nature) along the baseline-corrected curve are eliminated by this procedure.

3.3. Convolution method

The second step consists in extracting the RTD from $F_1^{mod}(t)$ and $F_2(t)$ curves. Although the CSTR$_4$ model is physically debatable when representing the inlet signal, it is a good candidate to model the liquid flow in the packed section. It allows calculating the response of the system in the Laplace domain as:

$$\overline{F_2^{mod}}(s) = \overline{F_1^{mod}}(s) \times \bar{E}(s) \tag{6}$$

where $\bar{E}(s)$ is the unknown RTD. Fitting leads to a new set of parameters t_m, K_{im}, J and t_M that is considered now as significant, and will deserve interpretation. A parameter regression identical to the one already described in Section 3.2 is used to minimize by the least squares method an objective function based on the experimental baseline-corrected F_2 (t) and the model $F_2^{mod}(t)$, this latter being the inverse Laplace transform of $\overline{F_2^{mod}}(s)$. It is noticeable that deconvolution is not involved; only the proper and stable convolution is used. Finally, the inverse Laplace transform of $\bar{E}(s)$ with its adjusted parameters gives access to the RTD function $E(t)$ using a Talbot algorithm.

Fig. 7 presents a typical example of this two-steps signal processing and the resulting RTD curve. A very good agreement is observed between baseline-corrected and modelled signals for the inlet and outlet positions. The next sections describe the results and interpretations of the parameters obtained using this procedure.

The overall impact of this novel treatment (image processing and RTD convolution) has been evaluated by comparing its responses with those obtained with the former envelope curve method. This comparison was done on three foam packings, namely 30, 40 and 50 PPI (see Table 2). Mean relative differences of nearly 0 to 8% are obtained for the first-order moment of the RTD whereas more pronounced deviations are obtained for the second-order moment, from 10 to 90%, confirming the necessity to re-investigate the RTD treatment.

4. Results & discussion

In this section, after a discussion on the experimental repeatability, the model ability to accurately represent the data is addressed. Finally residence time distributions and their moments are presented and analyzed for various liquid and gas flowrates and the different porous media.

4.1. Experimental repeatability

As explained in the experimental part, parameter uncertainty is estimated from the two inlet and two outlet signals recorded for a given set of experimental conditions. These signals lead to four different RTD (four different couples of inlet/outlet signals are possible). A stationary flow and a synchronous triggering of the video recording with the tracer injection are assumed. This was verified in most experiments except the ones at high liquid flow rates ($Q_L \geq 8$ mL/min) where the start off precision is not sufficient relatively to the short residence times obtained. In these cases, sufficiently repeatable mean residence times were not obtained and the results are therefore not considered as consistent in the following.

In the other cases, direct calculations of the first- and second-order moments of the four baseline-corrected curves (Eqs. (7)-(10)) are used to quantify the repeatability and to define what is called "experimental moments", contrary to Eqs. (2) and (3) that define "model moments":

$$\tilde{t}_i = \int_0^\infty [1 - F_i(t)]dt;\ i = (1,2) \tag{7}$$

$$\sigma_i^2 = \int_0^\infty [1 - F_i(t)]tdt - \tilde{t}_i^2;\ i = (1,2) \tag{8}$$

$$\tilde{t}_{exp} = \tilde{t}_2 - \tilde{t}_1 \tag{9}$$

$$\sigma_{exp}^2 = \sigma_2^2 - \sigma_1^2 \tag{10}$$

The experimental variability on the first- and second-order experimental moments of the RTD is quantified by representing their variation coefficients ($CV_{\tilde{t}_{exp}}$ and $CV_{\sigma^2_{exp}}$ respectively). They correspond to the ratio of the standard deviations with the average values for these two experimental moments. For the first-order moments (Fig. 8a), the average value of $CV_{\tilde{t}_{exp}}$ is 3% with a maximum value of 18% obtained for the shorter residence times (as discussed before). For the second-order moments (Fig. 8b), the average value of $CV_{\sigma^2_{exp}}$ is larger and is about 33% with a maximum value of 200% (only the residence times higher than 4 s were considered). These significantly higher values were expected for $CV_{\sigma^2_{exp}}$. Indeed, there is a systematic error induced by the uncertainty on the first-order moments $\tilde{t}$ when calculating σ^2_{exp}. Moreover, a flow disturbance due to tracer injection was noticed and appears as a source of variability in the second-order moment even if its impact on the first-order one is weaker. Overall, the mean residence time is properly determined when it exceeds 4 s and the variance can be considered qualitatively. Some ways to reduce the variability observed in the second-order moment would be to perform a larger number of experiments or alternatively and most probably to build a heavier experimental rig with two optical systems allowing the simultaneous acquisition of the inlet and outlet signals for a single injection.

4.2. Model validation

In Fig. 9, the values of the first- and second-order experimental moments of the RTD (Eqs. (9) and (10)) are compared to model moments (Eqs. (2) and (3)). For the first-order moment (Fig. 9a), a very good agreement is obtained between model and experimental values with less than 5% of deviation. The points are more scattered for the second-order moment σ^2 (Fig. 9b) with deviations up

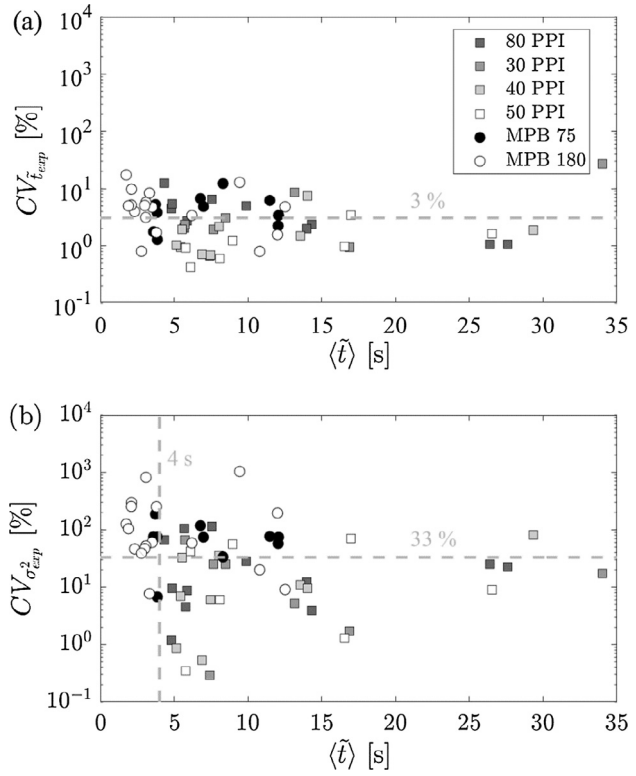

Fig. 8. Experimental variability estimation through Variation Coefficients (CV_i corresponding to the ratio of the relative standard deviation of i with the mean value of i) on (a) the first-order experimental moment and (b) the second-order experimental moment.

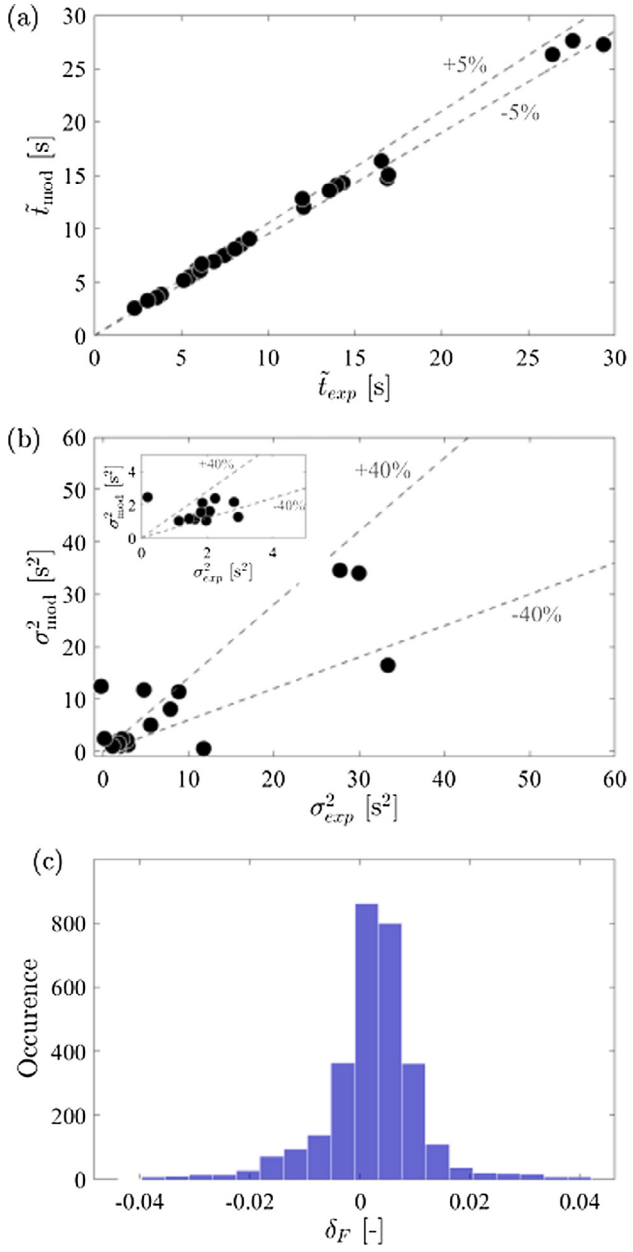

Fig. 9. Comparison of experimental and modelled (a) first and (b) second-order moments of the RTD; (c) Example of histogram of the residuals (δ_F) between the modelled curve by the CSTR$_4$ model, $F_2^{mod}(t)$, and the experimental cumulative curve with baseline correction, $F_2(t)$, [80 PPI foam, Q_G = 2 mL/min, Q_L = 4 mL/min].

to 40% (only a few ones exceed this value). These deviations between the model predictions and the experimental data are of the same order of magnitude as the experimental variability. This last result appears logical, even if the model is appropriate to represent faithfully the observed experimental results, it cannot reduce mathematically the experimental variability. Fig. 9c displays the distribution of the residuals (difference between F_2 and F_2^{mod}) for a given set of experimental conditions. The distribution is almost symmetrical and centered about 0, which suggests that the deviation between the model and the experiment is close to a random additive Gaussian noise. The low values of residuals indicate that the CSTR$_4$ model appears relevant to represent satisfactorily our data. Additional details about the uniqueness of the RTD parameter set are presented in Appendix A. As discussed earlier in Section 4.1, to improve the model validation concerning the second-order moment of the RTDs, the efforts should be experimental to suppress the tracer perturbation effects on them for future studies.

4.3. Effect of the gas and liquid flowrates

The effect of fluid flow rates is illustrated with the 80 PPI foam in Fig. 10. Fig. 10a and b present the impact of liquid flowrate Q_L on the RTD curves versus time and reduced time respectively, at a constant gas flowrate of 10 mL/min. Similarly, Fig. 10c and d display the dependence of the RTD on the gas flowrate at a constant liquid flowrate of 4 mL/min. It is easily observable on the temporal curves (Fig. 10a and c) that a decrease in liquid or gas superficial velocity leads to an increase in mean residence time and a spreading of the RTD. However, the impact of the liquid flowrate appears much more pronounced than that of the gas. To appreciate the effect of fluid flow rates on the dispersion independently of the mean residence time, the RTD in reduced time coordinate $E_R(\theta)$ has to be considered (Fig. 10b and d). It helps to see that an increase in the liquid or gas flowrate results both in a decrease in the liquid dispersive behavior with a reduction of the curve tail and asymmetry (mainly due to the exchange with stagnant zones). Fig. 10e and f show that the mean residence time and the reduced variance seem to depend monotonously on $1/u_L$ at constant u_G, with a slope strongly dependant on u_G. This trend seems no longer valid for the reduced variance at high u_G/u_L ratio. The qualitative behaviors described here for the impact of gas and liquid flowrates for the 80PPI foam were observed for the others porous media (see next section) and are common in other multiphase fixed bed reactors containing foams (Saber et al., 2012 and 2012a) or beads (Stegeman et al., 1996; Specchia and Baldi, 1977) especially for the mean residence time.

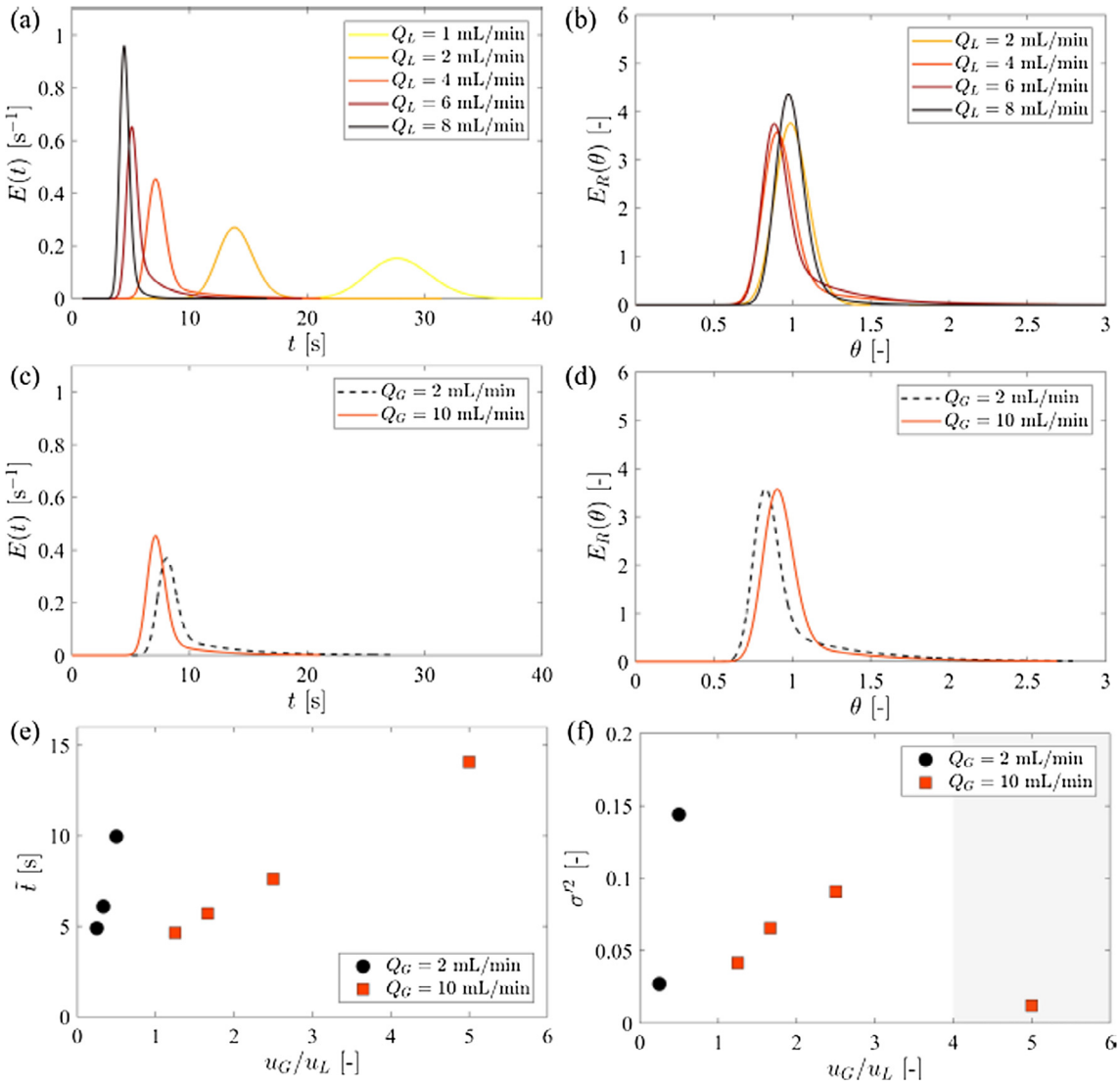

Fig. 10. Influence of the liquid and gas flow rates on the RTD [80 PPI foam]. Evolution of $E(t)$ (a) and $E_R(\theta)$ (b) for different Q_L [Q_G = 10 mL/min]. Evolution of $E(t)$ (c) and $E_R(\theta)$ (d) for different Q_G [Q_L = 4 mL/min]. Evolution of the mean residence time $\bar{t}$ (e) and reduced variance σ'^2 (f) with the ratio u_G/u_L of the gas and liquid superficial velocities.

4.4. Effect of the porous medium

A typical example of the impact of the porous medium on the RTD curves is presented in Fig. 11a and b for a given set of gas and liquid flowrates (Q_G = 2 mL/min and Q_L = 4 mL/min) in time (Fig. 11a) or reduced time coordinates (Fig. 11b). The large difference in bed porosity between foams and beads (≈90% vs ≈40%) is clearly visible in the RTD curves presented in time coordinate (Fig. 11a). When moving to the RTD curves expressed in reduced time (Fig. 11b), it is clear that foams display a broader RTD curve, which in addition is asymmetric with a longer tail than the two packed beds of spherical particles. It indicates that stagnant zones and their effect on the dispersion are more noticeable for these media. The noticeably different RTD curves of the 40 PPI and 80 PPI foams, that have the same mean pore diameter (see Table 2), indicate that this mean pore diameter is not enough to discriminate between 2 foams. The nature of the material (wettability) and other geometrical characteristics (porosity, strut shapes, node connectivity, occluded faces, orientation, etc.) have also to be considered.

To be able to compare the first moments of these RTD when looking at the impact of flowrates for example, it is appropriate to introduce the liquid saturation S_L, which considers only the accessible volume instead of the total reactor volume for the liquid hold-up ε_L.

$$S_L = \frac{\bar{t} Q_L}{\varepsilon V_R} = \frac{\varepsilon_L}{\varepsilon} \tag{11}$$

In Fig. 11c, the liquid saturation obtained for two foams (80 PPI and 40 PPI), a micro packed bed (MPB 75) and the empty channel are plotted as a function of the ratio of gas and liquid superficial velocities, u_G/u_L, for various couples of flowrates. Whatever the porous medium, its presence increases drastically the liquid saturation in comparison to the empty channel. What is less intuitive is that foams and packed beds, two very different bed structures, have the same level of liquid saturation and the same evolution with the ratio u_G/u_L. It is interesting to note, however, that the micro packed bed presents a slightly higher liquid saturation than foams under similar conditions. This second-order effect may probably result from differences in pore size, number and shape. A more detailed study would be necessary to quantify this effect further, with local characterization tools. Finally, when comparing all the porous media in terms of global dispersion, no clear correlation exists between the reduced variance of the liquid RTD, σ'^2,

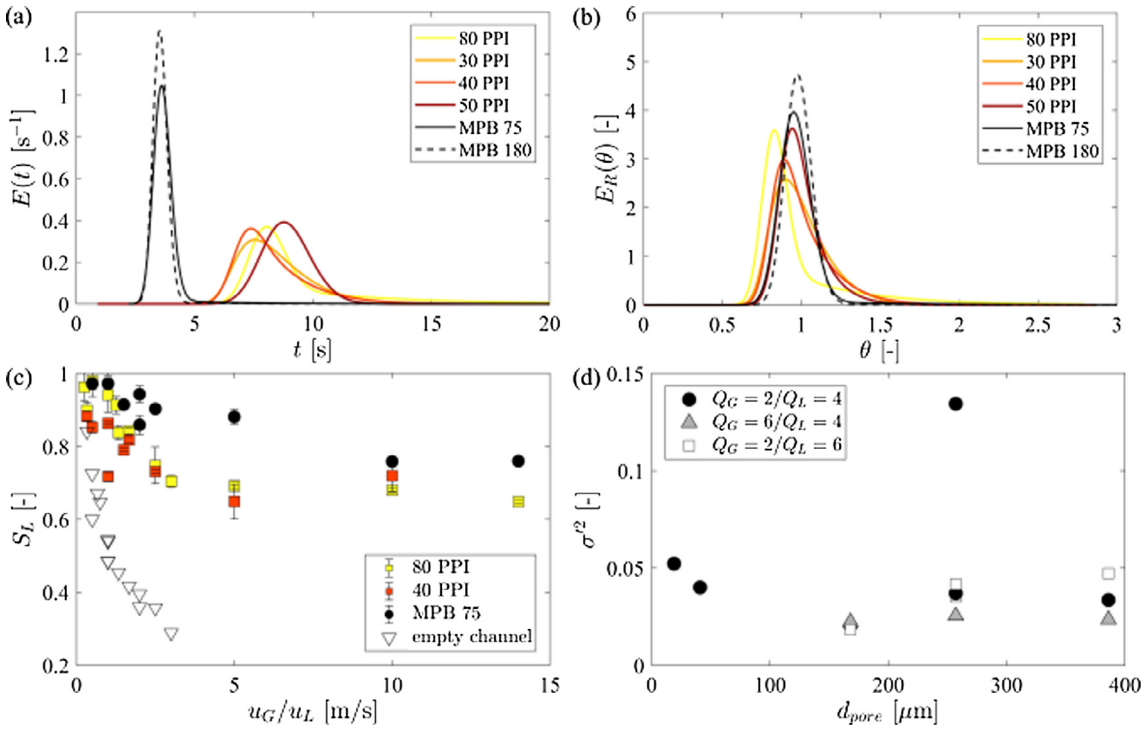

Fig. 11. Effect of the porous medium on $E(t)$ (a) and $E_R(\theta)$ (b) for identical flowrate conditions [Q_L = 4 mL/min; Q_G = 2 mL/min]. (c) Evolution of the liquid saturation S_L as a function of the ratio of gas and liquid superficial velocities u_G/u_L, for different porous media and without porous medium. (d) Evolution of the reduced variance σ'^2 with the mean pore diameter d_{pore} for various gas and liquid flowrates (Q_G and Q_L indicated in mL/min).

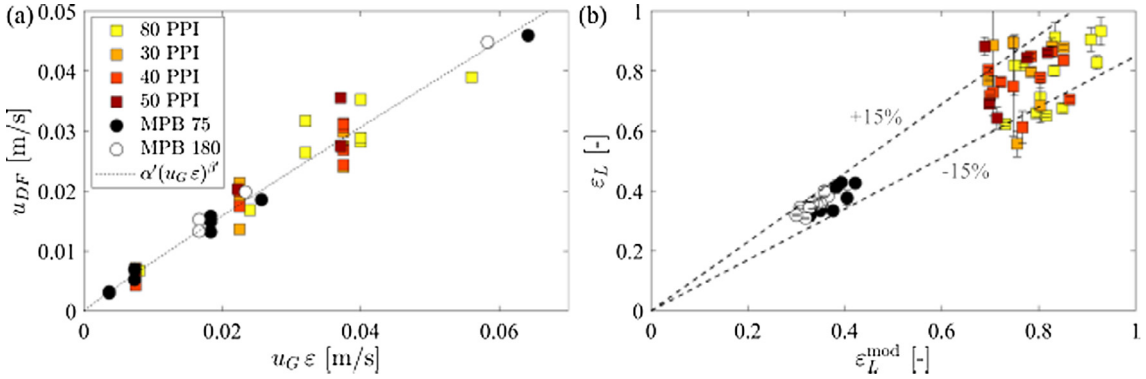

Fig. 12. Adaptation of the drift flux model to account for the fixed bed porosity. (a) Drift flux velocity, u_{DF}, as a function of the gas velocity, u_G, corrected by the bed porosity ε. (b) Parity plot of the corresponding liquid hold up estimations ($\varepsilon_L^{\mathrm{mod}}$ is the liquid hold up estimated from the drift flux model). The symbols indicating the different porous media are the same as in (a).

and the mean pore diameter, d_{pore}, of the porous media (Fig. 11d). This result is also counter-intuitive.

4.5. Drift flux model

In terms of a possible prediction of the mean liquid residence time for all the media (and the corresponding liquid hold up or saturation), one can try to go further in the chemical engineering approach in trying to merge all the results in a single correlation. As shown by Wallis (1962) and later by Darton and Harrison (1975), in two phase flows, each phase does not travel in the reactor with the same mean velocity, leading to the existence of a drift flux. This latter is the velocity of each dispersed units of gas slipping on the liquid. Darton and Harrison (1975) defined the drift flux in the framework of three phase fluidized beds. In this study, the solid phase is fixed, and the Darton and Harrison's expression has been modified accordingly. The drift flux velocity, hereafter named u_{DF}, depends on the liquid holdup, the porosity of the solid phase (ε) and the velocities of liquid (u_L) and gas (u_G) phases and is given by:

$$u_{DF} = u_G\varepsilon_L - u_L(\varepsilon - \varepsilon_L) \tag{12}$$

In fixed beds, as shown by Molga and Westerterp (1997), u_{DF} is mainly a function of u_G. Its dependence on u_L is negligible and a correlation of the following form is proposed:

$$u_{DF} = \alpha(u_G)^{\beta} \tag{13}$$

Their expression of u_{DF} was independent of the bed porosity because in dense fixed beds, the mean porosity is roughly constant and of about 40%. In the present study, the porous media have a very different porosity, and this parameter has to be considered. Therefore, a modified form with a dependency of the drift flux velocity upon gas superficial velocity and bed porosity is proposed as follows:

$$u_{DF} = \alpha'(u_G\varepsilon)^{\beta'} \tag{14}$$

As shown in Fig. 12a, all the porous media collapse on a single master curve according to this single expression involving only two fitted parameters (α', β'), as in the work of Molga and Westerterp (1997). Here the parameters take the following values: $\alpha' = 0.64$ and $\beta' = 0.94$. Introducing Eq. (14) into Eq. (12), provides a simple expression to predict the liquid holdup:

$$\varepsilon_L = \frac{\varepsilon u_L + \alpha'(u_G\varepsilon)^{\beta'}}{u_L + u_G} \tag{15}$$

As shown in Fig. 12b, all the experimental liquid hold ups (ε_L) can be predicted by equation 15 within ±15% with a mean relative deviation of 7% (the maximum deviation observed does not exceed 35%). Nonetheless, this correlation should be supported by a larger number of experiments, especially with a variety of fluid

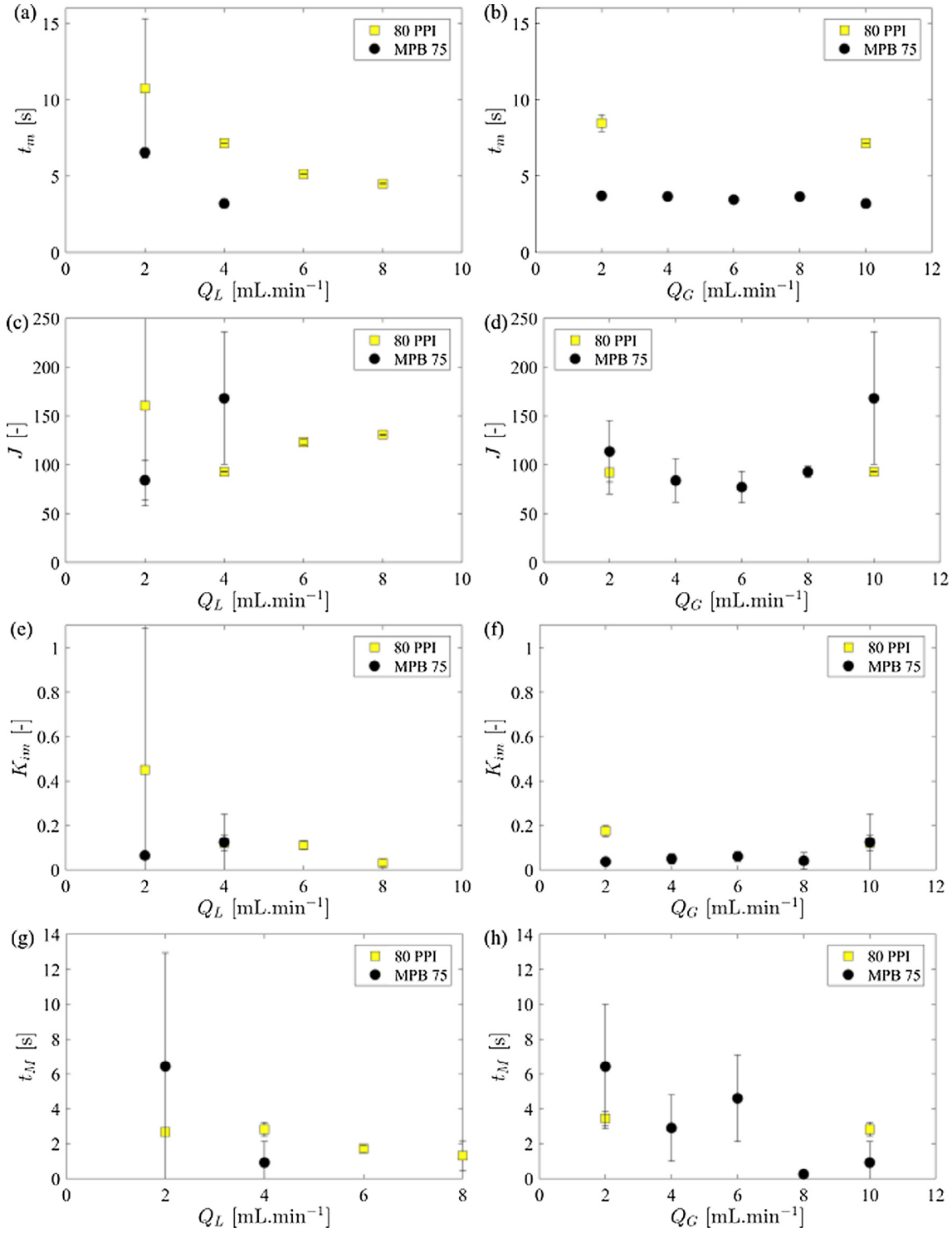

Fig. 13. Evolution of the CSTR$_4$ model parameters t_m (a, b), J (c, d), K_{im} (e, f) and t_M (g, h) as a function of liquid flow rate Q_L [(a, c, e, g), Q_G = 10 mL/min] and gas flow rate [(b, d, f, h), Q_L = 4 mL/min] for the 80 PPI foam and the micropacked bed MPB 75.

properties. Ideally, various channel sizes would also be necessary to tackle the impact of the degree of confinement.

4.6. Evolution of the model parameters and dispersion processes

In Fig. 13, the evolution of the four model parameters is represented as a function of the liquid (left column, Fig. 13a, c, e, g) and gas (right column, Fig. 13b, d, f, h) flowrates. Only two porous media (80 PPI foam and MPB75 micro-packed bed) are presented for the sake of clarity. Globally no clear and undebatable trend is noticeable. The gas flowrate seems to have a lower impact on the parameters than the liquid flowrate, except for t_M, for which the effect ~~is~~ seems comparable. This is in agreement with the RTD curves and their first- and second-order moments obtained in the study of the effect of flowrates (see Section 4.3). t_m and t_M may tend to decrease with an increase in liquid flowrate, which can be physically relevant. The two other parameters J and K_{im} seem pretty independent of flowrate variations and might be somehow intrinsic to the media (in the experimental domain investigated). J values are often much higher than 50 indicating a weakly dispersive flow in the dynamic zone. K_{im} values correspond to a fraction of stagnant liquid in the range of 10–20% which correspond to qualitative local observations and analysis of the flow (Serres et al., 2016; 2018).

Another way to discuss the parameters responses to physical variations is to consider them by regarding the characteristic times of the two hydrodynamic contributions to the dispersion as described in Sardin et al. (1991). Rearranging Eq. (3) leads to the following expressions for the dispersion time, t_D, and the mass transfer time, t_T:

$$\sigma'^2 = \frac{2}{t_m}(t_D + t_T) \tag{16}$$

$$t_D = \frac{t_m}{2J} \tag{17}$$

$$t_T = \frac{K_{im}}{(1+K_{im})^2} t_M \tag{18}$$

The variation of these two characteristic times with the gas and liquid flow rates are displayed in Fig. 14. At first sight it is noticeable that t_T is always one order of magnitude greater than t_D. It means that the transfer with the stagnant zones is dominant with respect to the dispersion in the dynamic zone and is controlling the overall dispersion. Again, it is physically interesting to notice that t_D is more sensitive to liquid flowrate than gas flow rate variations (Fig. 14a, b). t_T decreases with an increase in liquid or gas flowrate (Fig. 14c, d). Indeed, it is not direct and intuitive that reduced characteristic times are obtained with an increase of fluid velocity inside the porous medium, especially for the diffusion process.

Fig. 15 illustrates the effect of pore diameter on fitted model parameters and characteristic times for two couples of fluid flowrates. Concerning the model parameters (Fig. 15a-d), no clear tendency is observable. It can just be noticed that increasing d_{pore} might result in an increase of t_m and a decrease of t_M. Regarding the characteristic times (Fig. 15e-f), no particular tendency is noticeable. A higher t_D is obtained with foams than with packed beds. This observation is consistent with the more pronounced tails observed in the RTD for foams. Finally the tendency observed with the fluid flowrates is confirmed here regarding the predominant effect of mass transfer. The characteristic times obtained for dynamic dispersion are still one order of magnitude smaller than the characteristic times of the mass transfer between stagnant and dynamic zones.

5. Conclusions

An original method of liquid RTD acquisition adapted to small scale reactor is presented in details in this work. Its originality lies in its ability to handle pulsed signals often encountered in

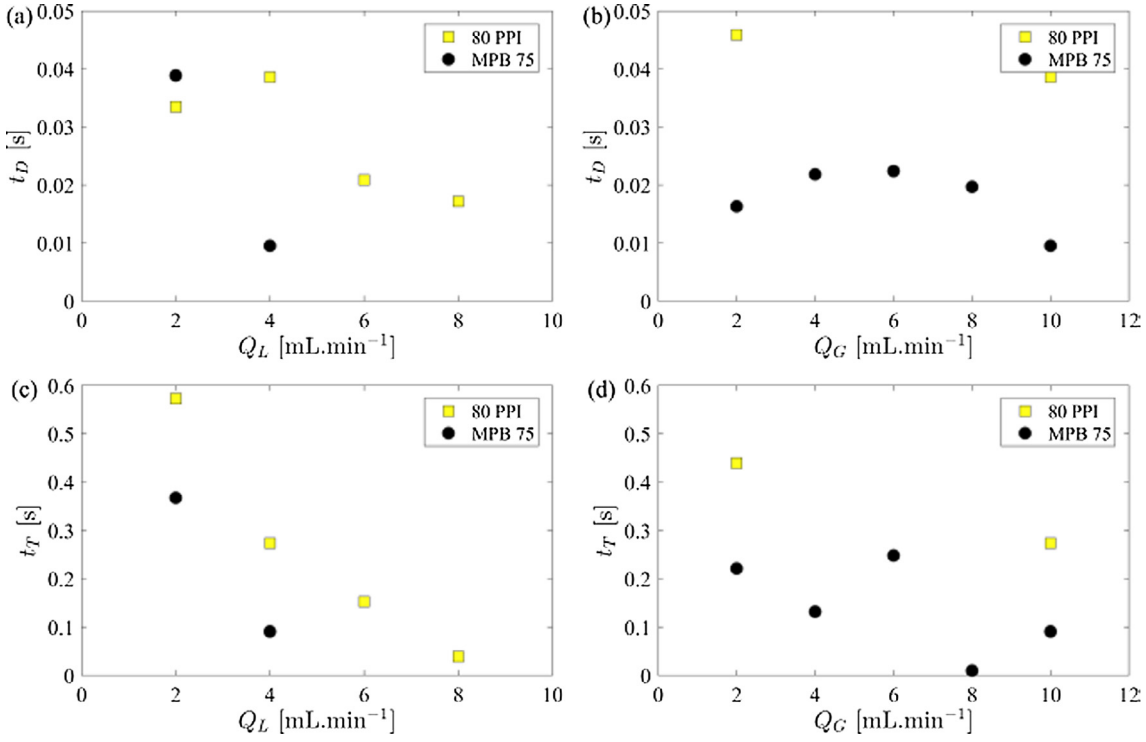

Fig. 14. Evolution of the characteristic time for dispersion in the dynamic zone, t_D (a, b) and the characteristic time for mass transfer between stagnant and dynamic zones, t_T (c, d) as a function of liquid flowrate, Q_L [(a, c), Q_G = 10 mL/min] and gas flow rate, Q_G [(b, d), Q_L = 4 mL/min] for the 80 PPI foam and the micropacked bed MPB 75.

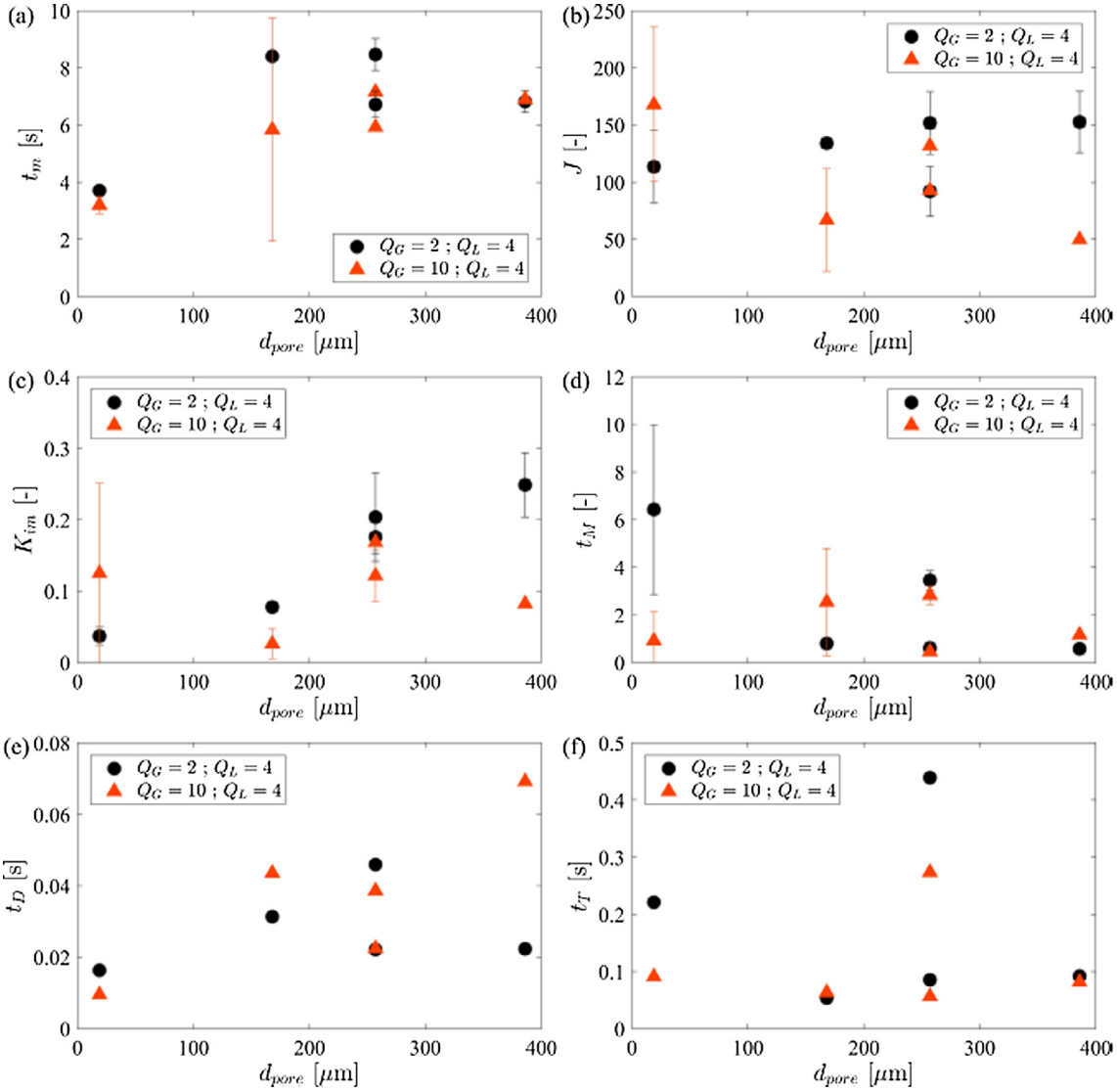

Fig. 15. Dependence of the model parameters t_m (a), J (b), K_{im} (c), t_M (d) and of the characteristic times (dispersion t_D (e) and transfer between zones t_T (f)) on the pore diameter d_{pore} for two given flow conditions [Q_G, Q_L indicated in mL/min].

multiphase flows at small scale and to be applicable as close as possible to the packing ends without inserting any dead volume. This method involving image analysis, global optimization and modelling steps, allows an accurate and robust access to the RTD curves. Fluid flowrates and bed structure effects were investigated for two different confined porous media of interest: dense MPBs and OCSFs. The method has been found highly robust to access the first-order moment of the RTD and a unique two-parameter correlation was adapted to predict successfully the similar trend of liquid saturation in the two packings. The model of Sardin et al. (1991) used in this study has been found sufficiently versatile to describe the dispersive behavior encountered and to explain it with a predominant effect of mass transfer with respect to convective dispersion. The global dispersive behavior of the liquid flow involving a stagnant liquid described here is in physical agreement with local observations of the flow inside the porous bed (Serres et al. 2018) where a liquid zone travelling slowly can coexist with a faster G-L two phase flow inside the complex porous structure. Improvement in the quantitative treatment of the second-order moments could be performed by a simultaneous acquisition of inlet and outlet signals.

Acknowledgements

This work was supported by the LABEX iMUST (ANR-10-LABX-0064) of Université de Lyon, with the program "Investissements d'Avenir" (ANR-11-IDEX-0007) operated by the French National Research Agency (ANR).

Appendix A. Uniqueness of the global optimization solution

Before discussing the values of the model parameters (t_m, J, K_{im}, and t_M), it is necessary to guaranty the uniqueness of the solution. To do so, we have developed a global optimization based on the "multistart" algorithm of Matlab™ (Mathworks®). This method is presented first, then, the statistical results of the modelling are briefly discussed.

The multistart algorithm consists in testing a large number of initial conditions ($t_{m,0}$, J_0, $K_{im,0}$, and $t_{M,0}$) as an input to the non-linear fitting and keeping the best solution. This method can be very time-consuming depending on the parameters space coverage. Therefore we defined reasonable bounds for each parameter,

based on preliminary tests and on the literature. Then, in order to cover the maximum of initial conditions possibilities with a reduced number of optimizations, we use the Latin Hypercube Sampling (LHS Design). An example of this homogeneous distribution of 500 initials points is displayed in Fig. A1a.

For a given set of initial conditions, a nonlinear fitting of the $CSTR_4$ model on the experimental points is performed as described in Section 3. Sometimes, the nonlinear fitting does not lead to a result (no convergence). It corresponds to the empty dots in Fig. A1a, which shows how the nonlinear fitting tool of Matlab™ (Mathworks®) combined to the $CSTR_4$ model is sensitive to the initial conditions. When the nonlinear fitting gave a result (convergence, filled dots in Fig. A1a), an objective function, $of = \sum (F_2^{mod}(t) - F_2(t))^2$ is calculated at the end of the fitting run to evaluate the accuracy of the $CSTR_4$ model, $F_2^{mod}(t)$, to represent the experimental points, $F_2(t)$. Values obtained for each set of initial conditions are reported in Fig. A1b, inset. The main plot of the Fig. A1b is a zoom of the inset around the minimum objective function value, of_{min}. Note that the minimum value of the objective function has a single occurrence, which proves the uniqueness of the solution.

For the sake of clarity, only the smaller values of the objective function *of* are represented in Fig. A2, as a function of the normalized parameters $p*$ of the $CSTR_4$ model. The uniqueness of the solution is proven by the single set of parameters corresponding to the smaller value of the objective function. Note that the objective function, *of*, decreases monotonically as a function of t_m and t_M, indicating the predominance of these two parameters in the optimization.

The variance-covariance matrix of the associated fitting is reported on Table A3a. The very small covariance between parameters seems to indicate that they are not correlated. To prove so, we represent in Table A3b the eigenvectors of this matrix. They are almost parallel to the axes defined by the four parameters, proving that these latter are not correlated. Hence, the system does not appear undersized, and the four parameters are relevant.

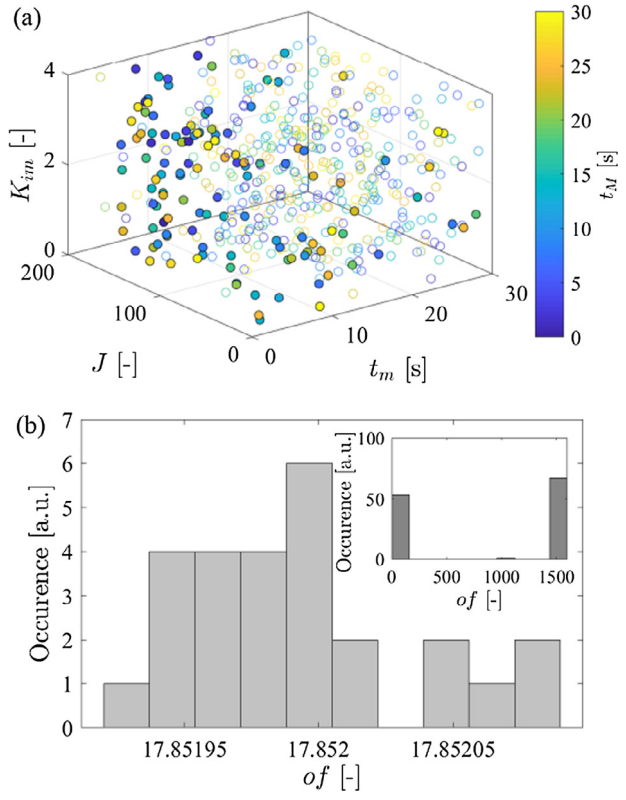

Fig. A1. (a) Distribution of the 500 initial conditions generated by the LHS Design in the parameter space. The empty points correspond to cases for which the non linear fitting does not converge; (b) Distribution of the best values of the objective function *of*. *Inset*: distribution of the objective function of for all points [foam 80 PPI, Q_G = 2 mL/min, Q_L = 4 mL/min].

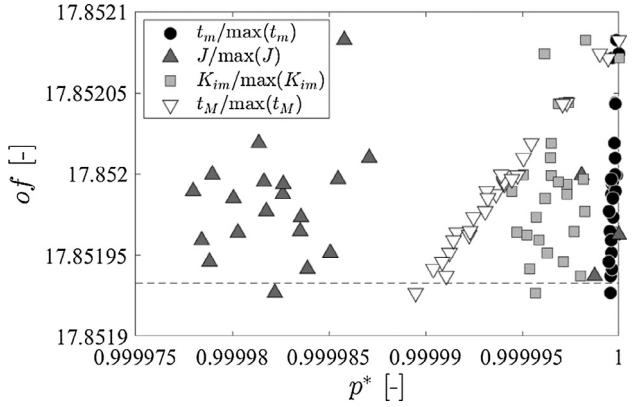

Fig. A2. Objective function *of* versus the normalized value p^* of the four model parameters (normalized by their maximum value). Only the minimum values of *of* are represented here for the sake of clarity. The dashed line indicates the limit below which a unique set of parameters exists which minimizes the objective function.

Table A3
(a) Variance-covariance matrix of the model parameters which optimize the RTD for the 500 initial conditions shown in Fig. A1. (b) Eigenvectors of the variance-covariance matrix in (a). These vectors are almost parallel to the axes defined by the parameters, showing that these latter are not correlated.

(a)

	t_m	J	K_{im}	t_M
t_m	13.3×10^{-6}	-20.3×10^{-6}	-1.3×10^{-6}	44.0×10^{-6}
J	-20.3×10^{-6}	1.5×10^{-1}	11.8×10^{-6}	-146.6×10^{-6}
K_{im}	-1.3×10^{-6}	11.8×10^{-6}	0.3×10^{-6}	-0.06×10^{-6}
t_M	44.0×10^{-6}	-146.6×10^{-6}	-0.06×10^{-6}	405.9×10^{-6}

(b)

$\vec{v_1}$	$\vec{v_2}$	$\vec{v_3}$	$\vec{v_4}$
1	-1.36×10^{-4}	1.53×10^{-1}	1.11×10^{-1}
3.93×10^{-5}	1	-7.40×10^{-5}	9.95×10^{-4}
-1.55×10^{-1}	-7.87×10^{-5}	1	-4.68×10^{-4}
-1.11×10^{-1}	9.80×10^{-4}	-1.65×10^{-2}	1

References

al-Rifai, N., Galvanin, F., Morad, M., Cao, E., Cattaneo, S., Sankar, M., Dua, V., Hutchings, G., Gavriilidis, A., 2016. Hydrodynamic effects on three phase micro-packed bed reactor performance – Gold–palladium catalysed benzyl alcohol oxidation. Chem. Eng. Sci. 149, 129–142.

Brun, E., Vicente, J., Topin, F., Occelli, R., 2008. Geometrical measurement of real foams from 3D images. Porous Metals Metallic Foams: METFOAM 2007, 425–428 (ISBN: 978-1-932078-28-2).

Butler, C., Cid, E., Billet, A.M., 2016. Modelling of mass transfer in Taylor flow: investigation with the PLIF-I technique. Chem. Eng. Res. Des. 115, 292–302.

Darton, R.C., Harrison, D., 1975. Gas and liquid hold-up in three-phase fluidisation. Chem. Eng. Sci. 30, 581–586.

de Klerk, A., 2003. Voidage variation in packed beds at small column to particle diameter ratio. Am. Inst. Chem. Eng. J. 49, 2022–2029.

de Loos, S.R.A., van der Schaaf, J., Tiggekaar, R.M., Nijhuis, T.A., de Croon, M.H.J.M., Schouten, J.C., 2010. Gas liquid dynamics at low Reynolds numbers in pillared rectangular microchannel. Microfluid. Nanofluid. 9, 131–144.

Danckwerts, P., 1953. Continuous flow systems: Distribution of residence time. Chem. Eng. Sci. 2, 1–13.

Deshmukh, S.R., Tonkovich, A.L.Y., Jarosch, K.T., Schrader, L., Fitzgerald, S.P., Kilanowski, D.R., Lerou, J.J., Mazanec, T.J., 2010. Scale-up of microchannel reactors for Fischer-Tropsch synthesis. Ind. Eng. Chem. Res. 49, 10883–10888.

Dittmar, D., Fredenhagen, A., Oei, S.B., Eggers, R., 2003. Interfacial tensions of ethanol–carbon dioxide and ethanol–nitrogen. Dependence of the interfacial tension on the fluid density–prerequisites and physical reasoning. Chem. Eng. Sci. 58, 1223–1233.

Elias, Y., von Rohr, P.R., 2016. Axial dispersion, pressure drop and mass transfer comparison of small-scale structured reaction devices for hydrogenations. Chem. Eng. Process. Process Intensif. 106, 1–12.
Faridkhou, A., Hamidipour, M., Larachi, F., 2013. Hydrodynamics of gas–liquid micro-fixed beds – Measurement approaches and technical challenges. Chem. Eng. J. 223, 425–435.
Faridkhou, A., Tourvieille, J.-N., Larachi, F., 2016. Reactions, hydrodynamics and mass transfer in micro-packed beds—Overview and new mass transfer data. Chem. Eng. Process. Process Intensif. 110, 80–96.
Glover, P.W., Walker, E., 2009. Grain-size to effective pore-size transformation derived from electrokinetic theory. Geophysics 74, E17–E29.
Häfeli, R., Hutter, C., Damsohn, M., Prasser, H.M., von Rohr, P.R., 2013. Dispersion in fully developed flow through regular porous structures: Experiments with wire-mesh sensors. Chem. Eng. Process. Process Intensif. 69, 104–111.
Hutter, C., Zenklusen, A., Lang, R., Rudolf, P.h., von Rohr, 2011. Axial dispersion in metal foams and streamwise-periodic porous media. Chem. Eng. Sci. 66, 1132–1141.
Iliuta, I., Larachi, F., Grandjean, B.P.A., 1999. Residence time, mass transfer and back-mixing of the liquid in trickle flow reactors containing porous particles. Chem. Eng. Sci. 54, 4099–4109.
Inoue, T., Schmidt, M.A., Jensen, K.F., 2007. Microfabricated multiphase reactors for the direct synthesis of hydrogen peroxide from hydrogen and oxygen. Ind. Eng. Chem. Res. 46, 1153–1160.
Inoue, T., Adachi, J., Ohtaki, K., Lu, M., Murakami, S., Sun, X., Wang, D.F., 2015. Direct hydrogen peroxide synthesis using glass microfabricated reactor – Paralleled packed bed operation. Chem. Eng. J. 278, 517–526.
Kreutzer, M.T., Bakker, J.J.W., Kapteijn, F., Moulijn, J.A., Verheijen, P.J.T., 2005a. Scaling-up multiphase monolith reactors: linking residence time distribution and feed maldistribution. Ind. Eng. Chem. Res. 44, 4898–4913.
Kreutzer, M.T., Kapteijn, F., Moulijn, J.A., Heiszwolf, J.J., 2005b. Multiphase monolith reactors: Chemical reaction engineering of segmented flow in microchannels. Chem. Eng. Sci. 60, 5895–5916.
Kreutzer, M.T., Günther, A., Jensen, K.F., 2008. Sample Dispersion for Segmented Flow in Microchannels with Rectangular Cross Section. Anal. Chem. 80, 1558–1567.
Kulkarni, A.A., Kalyani, V.S., 2009. Two-phase flow in minichannels: hydrodynamics, pressure drop, and residence time distribution. Ind. Eng. Chem. Res. 48, 8193–8204.
Lerou, J.J., Tonkovich, A.L., Silva, L., Perry, S., McDaniel, J., 2010. Microchannel reactor architecture enables greener processes. Chem. Eng. Sci. 65, 380–385.
Liu, Y., Edouard, D., Nguyen, D.L., Begin, D., Nguyen, P., Pham, C., Pham-Huu, C., 2013. High performance structured platelet milli-reactor filled with supported cobalt open cell SiC foam catalyst for the Fischer-Tropsch synthesis. Chem. Eng. J. 222, 265–273.
Losey, M., Schmidt, M.A., Jensen, K.F., 2001. Microfabricated multiphase packed-bed reactors: characterization of mass transfer and reactions. Ind. Eng. Chem. Res. 40, 2555–2562.
Márquez, N., Castaño, P., Makkee, M., Moulijn, J.A., Kreutzer, M.T., 2008. Dispersion and Holdup in Multiphase Packed Bed Microreactors. Chem. Eng. Technol. 31, 1130–1139.
Molga, E.J., Westerterp, K.R., 1997. Experimental study of a cocurrent upflow packed bed bubble column reactor: pressure drop, holdup and interfacial area. Chem. Eng. Process. 36, 489–495.
Moulijn, J.A., Makkee, M., Berger, R.J., 2016. Catalyst testing in multiphase micro-packed-bed reactors; criterion for radial mass transport. Catal. Today 259, 354–359.
Mueller, G.E., 1991. Prediction of radial porosity distributions in randomly packed fixed beds of uniformly sized spheres in cylindrical containers. Chem. Eng. Sci. 46, 706–708.
Papageorgiou, J.N., Froment, G.F., 1995. Simulation models accounting for radial voidage profiles in fixed-bed reactors. Chem. Eng. Sci. 50, 3043–3056.
Plucinski, P.K., Bavykin, D.V., Lapkin, A.A., Kolaczkowski, 2005. Liquid-phase oxidation of organic feedstock in a compact multichannel reactor. Ind. Eng. Chem. Res. 44, 9683–9690.
Potdar, A., Protasova, L.N., Thomassen, L., Kuhn, S., 2017. Designed porous milli-scale reactors with enhanced interfacial mass transfer in two-phase flows. React. Chem. Eng. 2, 137–148.
Saber, M., Pham-Huu, C., Edouard, D., 2012. Axial Dispersion Based on the Residence Time Distribution Curves in a Millireactor Filled with β-SiC Foam Catalyst. Ind. Eng. Chem. Res. 51, 15011–15017.
Saber, M., Truong-Huu, T., Pham-Huu, C., Edouard, D., 2012a. Residence time distribution, axial liquid dispersion and dynamic–static liquid mass transfer in trickle flow reactor containing β-SiC open-cell foams. Chem. Eng. J. 185–186, 294–299.
Sardin, M., Schweich, D., Leij, F., Vangenuchten, M., 1991. Modeling the non-equilibrium transport of linearly interacting solutes in porous-media - a review. Water Resour. Res. 27, 2287–2307.
Serres, M., Zanota, M.-L., Philippe, R., Vidal, V., 2016. On the stability of Taylor bubbles inside a confined highly porous medium. Int. J. Multiph. Flow 85, 157–163.
Serres, M., Maison, T., Philippe, R., Vidal, V., 2018. A phenomenological model for bubble coalescence in confined highly porous media. Int. J. Multiphase Flow. 10.1016/j.ijmultiphaseflow.2018.04.0030301-9322/.
Specchia, V., Baldi, G., 1977. Pressure drop and liquid holdup for two phase concurrent flow in packed beds. Chem. Eng. Sci. 32, 515–523.
Stegeman, D., van Rooijen, E., Kamperman, A., Weijer, S., Westerterp, K.R., 1996. Residence time distribution in the liquid phase in a cocurrent gas liquid trickle bed reactor. Ind. Eng. Chem. Res. 35, 378–385.
Tourvieille, J.-N., Philippe, R., de Bellefon, C., 2015. Milli-channel with metal foams under an applied gas–liquid periodic flow: Flow patterns, residence time distribution and pulsing properties. Chem. Eng. Sci. 126, 406–426.
Tourvieille, J.-N., Philippe, R., de Bellefon, C., 2015a. Milli-channel with metal foams under an applied gas–liquid periodic flow: External mass transfer performance and pressure drop. Chem. Eng. J. 267, 332–346.
Trachsel, F., Gunther, A., Khan, S., Jensen, K.F., 2005. Measurement of residence time distribution in microfluidic systems. Chem. Eng. Sci. 60, 5729–5737.
van Herk, D., Kreutzer, M.T., Makkee, M., Moulijn, J.A., 2005. Scaling down trickle bed reactors. Catal. Today 106, 227–232.
van Herk, D.A., Castaño, P., Makkee, M., Moulijn, J.A., Kreutzer, M.T., 2009. Catalyst testing in a multiple-parallel, gas–liquid, powder-packed bed microreactor. Appl. Catal. A 365, 199–206.
Varas, G., Vidal, V., Géminard, J.-C., 2011. Venting dynamics of an immersed granular layer. Phys. Rev. E 83, 011302.
Villermaux, J., 1987. Chemical engineering approach to dynamic modeling of linear chromatography, A flexible method for representing complex phenomena from simple concepts. J. Chromatogr. 406, 11–26.
Wallis, G.B., 1962. One dimensional two phase flow. McGraw Hill.
Wen, C.Y., Fan, L.T., 1975. Models for flow systems and chemical reactors. Marcel Dekker, New York. 1975.
Yang, L., Shi, Y., Abolhasani, M., Jensen, K.F., 2015. Characterization and modeling of multiphase flow in structured microreactors: a post microreactor case study. Lab. Chip. 15, 3232–3241.